Improved degassing efficiency and mechanical properties of A356 aluminium alloy castings by high shear melt conditioning (HSMC) technology

Jaime Lazaro-Nebreda[1,2], Jayesh B. Patel[1] and Zhongyun Fan[1]

[1] Brunel Centre for Advanced Solidification Technology, Brunel University London, Uxbridge, UB8 3PH, United Kingdom.

[2] Corresponding author: jaime.lazaronebreda@brunel.ac.uk

Abstract

The degassing of aluminium alloy melts is a crucial step in the production of high-quality casting products, as the presence of dissolved hydrogen and oxide bi-films is detrimental to the mechanical properties. Current rotary degassing techniques are effective, but they lack efficiency because of the high gas flow and long processing times required. This study aims to solve this problem by presenting an innovative rotor-stator degassing technology, that combines controlled inert gas injection with intensive melt shearing. It has been applied to the liquid metal treatment of an aluminium cast alloy to evaluate the effect on melt cleanliness, casting integrity and mechanical properties. The optimum conditions for an efficient bubble dispersion have been obtained by water modelling. The melt quality during and after degassing has been assessed by in-situ measurement of hydrogen concentration and by reduced pressure test sampling for oxide bi-films and porosity content evaluation. This new technology is faster, requires less gas flow consumption and produces higher melt quality than the existing degassing techniques, due to a characteristic combination of distributive and dispersive mixing flow. In addition, re-gassing is minimised, maintaining a high melt quality for longer time after processing. This results in castings with less defects and better mechanical properties. The improved degassing efficiency of this technology makes it an excellent alternative in industry to increase melt quality and casting productivity.

Keywords: Aluminium alloy, high shear melt conditioning, degassing, oxide bi-film, mechanical properties, casting defects

1. Introduction

Aluminium alloys are widely used in various industrial sectors for the purpose of weight saving and because of the excellent combination of properties, as reported by Polmear (1995) However, the presence of porosity in the final casting components is quite common and has a detrimental effect on the mechanical properties, especially the elongation and tensile strength, as reported by Caceres and Selling (1996) and the fatigue behaviour, as reported by Ammar et al. (2008). Porosity originates during the solidification stage and once formed it is difficult to remove either by heat treatments or deformation processing, as reported by Chaijaruwanich et al. (2007). It is therefore necessary to ensure a good melt quality before casting by eliminating, or at least reducing, the causes of porosity.

Campbell (2003) mentioned two major factors that determine the quality of an aluminium melt. One is the presence of oxide films with poor wettability and the other is the dissolved hydrogen. Both are consequence of reaction of the liquid aluminium with the ambient water moisture, as described in Eq. 1, producing atomic hydrogen, that quickly dissolves in the melt, and alumina that is deposited in the surface as a thin layer. When the melt is disturbed during melt handling, the layer breaks and folds over, forming a so called bi-film oxide that becomes entrained inside the melt.

$$2Al + 3H_2O \rightarrow Al_2O_3 + 6H \quad (1)$$

Hydrogen has been normally considered the origin for gas porosity in aluminium, because of the much lower solubility in solid than in liquid. During solidification, the excess of hydrogen is rejected from solution, and recombines as molecular gas in the interdendritic regions. Campbell (2003) suggested, however, that the oxide bi-films play a more important role in the formation of gas porosity. Each oxide bi-film present two sides, the outer is the wet side in contact with the liquid and the inner is the dry side in contact with entrapped air. Dispinar and Campbell (2004) described that during the solidification, the bi-film unfolds and any hydrogen in excess in the melt automatically diffuses into the gap within the bi-film sides. Tiryakioglu (2020) has recently shown that hydrogen gas porosity can not nucleate in liquid aluminium and therefore the initiator of porosity is the bi-film, with the hydrogen just acting as an agent that makes defects more visible by contributing to the pore expansion. Therefore, not only the hydrogen but, more importantly, the bi-films should be removed during the degassing process before casting to reduce its potency to form porosity during solidification.

Zhang et al. (2011) reviewed current methods for degassing molten aluminium that are in industrial use or under research and development, which include the injection of inert or reactive gas with lances or porous plugs, flux addition, vacuum degassing, ultrasound degassing, spray degassing and rotary degassing. Among them, the most popular method used in industry is rotary degassing, because of its simple implementation and good performance in comparison with the other techniques. In rotary degassing, the smaller and the better distributed the gas bubbles are, the higher the degassing efficiency. Warke et al. (2005a) and Warke et al. (2005b) found that increasing rotor speed reduces the size of the bubbles and accelerates hydrogen removal, but also causes surface turbulence and a vortex, which accelerates the reabsorption of hydrogen (re-gassing) and the entrapment of new oxide films in the melt. Therefore, the rotor speed cannot be too high in conventional rotary degassing. Baffles are normally used in industry to prevent vortex appearance but are only effective to certain extent and for small melts. Camacho-Martinez (2010) suggested that increasing gas flow rate could decrease the vortex size by affecting the fluid flow around the impeller and Hernandez-Hernandez et al. (2015) found that increasing gas flow rate can also speed up the degassing process. However, Zuo et al. (2016) reported that above a certain gas flow rate the process efficiency decreases as bubbles escape too fast to the surface. This reduces the collection of hydrogen and can also cause severe surface turbulences. Therefore, the gas flow rate is also limited in conventional rotary degassing in terms of process efficiency.

Current research on rotary degassing is focused on computer modelling to assist process condition optimization and on the re-design of the rotary impeller. In that sense, Hernandez-Hernandez et al. (2016) proposed a modified impeller design that can help in better distribution of bubbles, as well as reducing processing time and, with it, gas consumption between 14% and 34% compared with commercial designs, while Wan et al. (2018) recommended the variation of immersion depth of the impeller for the same purpose. Despite these efforts, rotary degassing efficiency is still not high enough mainly due to the need for relatively high gas flow rates and the long processing times of 20-30 mins for lowering the hydrogen content to industrially accepted levels. Moreover, Mostafei (2016) reported that the operating window in which rotary degassing produces good results is small and that a wrong combination of process conditions may result in no improvement or even degradation in quality of

castings. More recent study by Gyarmati et al. (2020) reported that without flux addition, rotary degassing is only effective at removing hydrogen, but not the oxide bi-films in the melt.

Regarding this issue, Fan et al. (2009) demonstrated that melt conditioning by an advanced shear technology can effectively disperse oxide films into fine individual particles, and Zuo et al. (2011) reported that when used in combination with Ar gas, intensive melt shearing has a significant degassing effect on aluminium alloys. Based on this principle, Fan et al. (2011) developed a novel rotor-stator high shear degassing technology, which allows the rotation speed to be increased without vortex generation. This new technology was initially tested by Zuo et al (2013) in molten A356 alloy and later by Zuo et al. (2015) and Kang et al. (2015) in molten A7032 alloy, finding in all cases a significant reduction in hydrogen and in oxide bi-film content when compared to conventional rotary degassing. Furthermore, they analysed the possibilities of this novel technology and discussed the potential economic benefits when implemented in industry for improving the integrity of the castings. Lazaro-Nebreda et al. (2018) continued the investigations on the HSMC technology for melt purification purposes and reported on the importance of reducing the inlet gas flow in the degassing process to achieve a better bubble dispersion and degassing efficiency. These previous results have been included in this paper (section 3.1) with a more detailed discussion. However, no mechanical properties were reported in any of those previous studies. Recently, Zhang et al. (2018) found that the use of high shear melt conditioning after degassing reduces the variation of the mechanical properties of HPDC components based on the A380 alloy, via oxide dispersion and enhanced grain nucleation during solidification, and Lordan et al. (2019) found that it also helps reducing the size and amount of porosity and defects in the HPDC castings. However, no significant increment on the mechanical properties was observed in these studies because of the inevitable high level of defects originated during this casting process, as recently reported by Zhang et al. (2020).

Despite the observed potential of the high shear melt conditioning technology, the available information about the most efficient degassing conditions in terms of gas flow and rotor speed, is limited. Moreover, the full details of the effect of the melt quality after high shear degassing on the mechanical properties has not yet been evaluated. Therefore, the aim of the present work is to fill this gap of knowledge and compare process efficiency with that obtained with conventional degassing methods, such as tablet fluxing and rotary degassing. This includes physical modelling in water to assess

the effect of gas flow and rotation speed on bubble dispersion, the in-situ measurement of melt quality during and after degassing, and the evaluation of mechanical properties and integrity of components produced by gravity die casting at different times after the melt treatment.

2. Experimental procedure

2.1. Material melting and casting process

The secondary aluminium cast alloy A356, with composition Al-6.87Si-0.36Mg-0.12Fe (wt.%), was used in this study. The alloy was melted in charges of 10 kg ingots in three clay graphite crucibles (salamander A25; top diameter of 210mm, bottom diameter of 155mm and height of 280mm) in an electrical resistance furnace at a temperature of 700 ± 5 °C. One hour after homogenisation each batch of melt was degassed using a different method (section 2.2). After degassing, the melts were skimmed and held isothermally in the furnace for up to 60 min. No granular flux was used to cover and protect the surface of the melt to allow natural re-gassing to occur during the holding period. The melt quality was assessed at different times, both during degassing and holding stages, by standard techniques (section 2.3). Additionally, tensile bars were cast at certain times during the holding stage to evaluate the effect of each melt treatment on the mechanical properties (section 2.4) and on the as-cast microstructure (section 2.5).

2.2. Degassing methodology

The objective of the study was to evaluate the effect of the new high shear degassing technology, but to avoid bias and for comparison purposes, three degassing methods were used during this investigation, one on each crucible. In the first crucible, degassing was done by adding 0.2wt.% of degassing tablet (FOSECO Nitral C19) into the melt, using a bell degassing plunger to push the tablet to the bottom of the crucible. The plunger was withdrawn when the bubbling at the surface stopped completely (~5min). The second crucible was degassed using a commercial rotary degasser (FOSECO, ϕ90mm) for 10 min. The impeller was immersed near the bottom of the crucible (~50 mm) and operated at a stirring speed of 350 rpm and an Ar flow rate of 5 L/min. The third melt was processed using the innovative high shear melt conditioning (HSMC) degassing technology developed at BCAST (section 2.2.1) during 10 min. The unit was immersed halfway from melt surface to the bottom of the crucible

(~125 mm) and operated at a rotor speed of 3000 rpm and Ar flow rate of 0.1 L/min. These processing parameters were selected after physical modelling in water for obtaining efficient conditions for bubble dispersion (section 2.2.2).

2.2.1. High shear melt conditioning (HSMC) degassing technology

The high shear melt conditioning (HSMC) technology developed at BCAST by Fan et.al. (2011) comprises of a rotor-stator arrangement made from an inert ceramic material. The HSMC model used in this study, HSM-40-AL (**Fig. 1a**), is the same that Zuo et al. (2013) used in the initial development of the high shear degassing technology and further studies. The rotor has four blades forming a cross, with a diameter of 29.5 mm. The stator outer and inner diameters are 42 mm and 30 mm, respectively. This gives a small gap of 0.25 mm between the rotor blades and the inner wall of the stator. The stator openings are disposed as 4 rows of 16 circular holes of 2.5 mm diameter uniformly distributed around the stator perimeter.

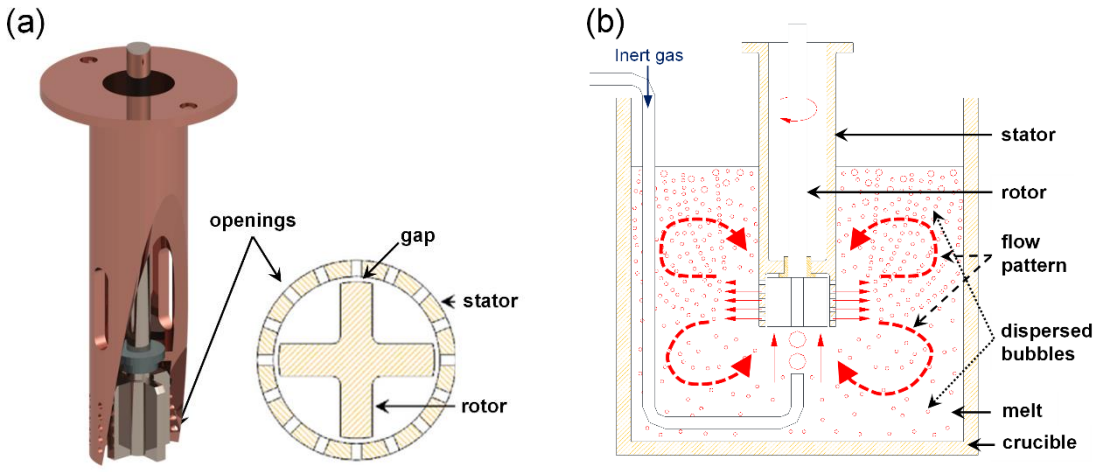

Fig. 1. Schematic of the rotor-stator HSMC unit. (a) lateral and bottom view, (b) inside a melt illustrating the degassing procedure.

During its operation in molten metal (**Fig. 1b**) the rotation speed can vary in the range of 1000-10000 rpm, providing an extremely high shear rate (up to 10^4-10^5 s^{-1}). This high shear rate is the result of the melt being pumped upwards from the bottom and then squeezed in between the small rotor-stator gap and through the openings of the stator. The liquid is projected radially, as high velocity jets, towards the

wall of the crucible where it splits into upper and lower flow patterns (dashed arrows in **Fig. 1b**), while more liquid is being pumped into the unit. Therefore, the technology provides not only macro-flow in a large volume of melt for distributive mixing, but also micro-flow with intensive shearing effect near the tip of the device for dispersive mixing.

In the HSMC degassing technology, the gas is injected into the melt by an external pipe (4 mm inner diameter) placed 20 to 30 mm underneath the unit (**Fig. 1b**). Camacho-Martinez et al. (2012) reported that the use of gas injection underneath the impeller with an external pipe, instead of through the shaft, improves the bubble distribution in rotary degassing and allows the gas flow rate to be reduced, as required. This way, the incoming bubbles are captured by the rotor spinning, which creates a pumping action, and are then subjected to intensive shearing and dispersed into many tiny bubbles when they pass through the stator openings and are distributed through the whole melt following the macroscopic flow pattern provided by the high velocity jets.

2.2.2. Physical modelling of the degassing process in water

To visualize how the bubble dispersion occurs with the use of the HSMC degassing technology, controlled tests were done prior to melt treatment using a transparent glass tank (base 210 mm) and two modelling HSM-40-AL units made of plastic. The tank was filled with water (~250 mm height) and the unit was immersed halfway below the liquid surface. The gas pipe end was placed 30 mm below the unit and the tests were carried out by operating the unit at different rotor speeds and under varied Ar gas flow rates. Two gas flow rates were studied, 1 L/min (high rate) and 0.1 L/min (low rate), and the rotor speed was increased from 1000 to 6000 rpm. The process was recorded using a digital camera.

Regarding the applicability of the results found in this section for the degassing of aluminium melts, it should be noted that recent studies by Tzanakis et al. (2017) and Yamamoto et al. (2018) have reported that water shares similar fluid and dynamic behaviour (viscosity to density ratio) with molten aluminium and is the most appropriate liquid to replicate bubble dispersion and degassing performance in molten aluminium. In the working range, above 1000 rpm, the HSMC mixer flow is always in the turbulent regime both in water or aluminium, i.e., the Reynolds number is $Re > 10^4$, with it defined by $Re = \rho ND^2/\mu$ as in Hakanson (2018), where ρ is the fluid density and, μ is the fluid viscosity, N is the rotor speed and D is the characteristics length, here the rotor diameter.

Furthermore, the crucibles used for the aluminium melt treatment were chosen to be of similar dimensions to the glass tank employed during the bubble dispersion observations in water. This way the bubble dispersion behaviour in liquid aluminium is expected to be similar to what is observed in water and the results obtained in section 3.1 with water modelling (rotor speed and gas flow) could be directly implemented in the aluminium melt processing as shown from section 3.2.

2.3. Melt quality evaluation

The hydrogen concentration in the melts, before, during and after the degassing melt treatments, was directly measured by using a FOSECO ALSPEK-H probe. The probe was immersed at a depth of between 150 and 200 mm in the melt. The readings were given in $cm^3/100g$ with real time data.

The reduced pressure test (RPT) was also considered in this study. The method involves solidifying the melt into two conical steel cups, one in air (atmospheric pressure) and the other under partial vacuum (80mbar or 8 kPa). The cups were always preheated above 200 °C prior to each test to prevent rapid solidification and ensure reliable results, as recommended by Tan et al. (2011). The melt quality was accessed by using the density index (DI), which was calculated using Eq. 2, where D_{air} and D_{vac} are the density of samples solidified in air and under vacuum, respectively.

$$DI = (D_{air} - D_{vac}) / D_{air} \quad (2)$$

After calculating the density index, selected samples were sectioned, ground and polished to evaluate the porosity size and distribution by using the image analysis software ImageJ.

2.4. Tensile property evaluation

Following each degassing treatment, sets of tensile bars were cast at certain times (10 min, 30 min and 50 min) during the isothermal holding stage by manually pouring with a ladle into an ASTM B108 standard permanent steel mould (ASTM, 2019). **Fig. 2a** shows the geometry of the mould used, with arrows indicating the nominal flow of liquid metal. In total, 12 tensile specimens were produced from each melt (4 at each holding time), with the key dimensions shown in **Fig. 2b**. Care was taken to pour the material under the same conditions each time, by keeping the mould preheated inside a furnace at 460 °C before each casting, as reported by Dong et al. (2018).

After being kept at ambient temperature for 24h, the tensile specimens were tested in the as-cast condition at room temperature using an Instron 5500 universal electromechanical testing system equipped with a 50kN load cell, in accordance with ASTM standard E8-03 (ASTM, 2003). The yield strength at 0.2% offset (Ys), the ultimate tensile strength (UTS) and the elongation at break (El%) were evaluated from the stress-strain curves. Each data and standard deviation reported in the results was based on properties obtained from the 4 samples cast each time.

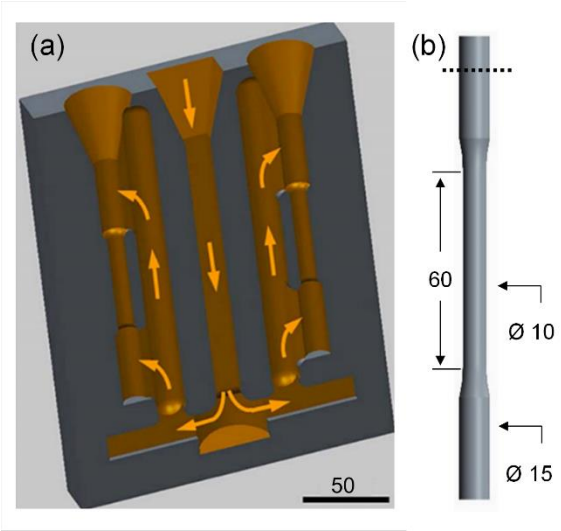

Fig. 2. (a) Geometry of the standard ´Stahl´ mould used to produce tensile specimens according to ASTM B108 (arrows indicate the nominal flow of the liquid metal); (b) tensile specimen geometry and dimensions (dotted line indicate region for pre-test microstructure evaluation). Dimensions in mm.

2.5. Microstructure characterization

Selected tensile specimens were examined for microstructure and porosity, both before and after tensile testing, to better understand the nature of the mechanical failure. For the pre-test characterization, a slice was cut from the top part of the sample (location marked with a dotted line in **Fig. 2b**). The tested specimens were examined at the location of fracture. Samples were prepared by standard metallographic techniques. Microstructure images were acquired using a Zeiss optical microscope and analysed using ImageJ software.

3. Results and discussion

3.1. Effect of HSMC on bubble dispersion by water modelling

Fig. 3 shows a selection of the most representative snap-shots from the videos recorded during the water experiments under different conditions. Dashed arrows have been included in the images to indicate the bubble flow path and allow for a better observation of the region affected by the dispersed bubbles. For the higher gas flow rate (1 L/min) and 2000 rpm, it can be observed in **Fig. 3a** how the large bubbles (10-20 mm) leaving the incoming pipe were captured by the rotor-stator unit and came out of the stator holes as high velocity air-water jets containing smaller size bubbles (< 1 mm). These bubbles then followed a parabolic trajectory and travelled fast upwards and disturbed the surface similarly to what happens in commercial rotary degassing. No vortex formation is observed, even though the rotor speed is much higher than what is normally used with conventional rotary degassers (~500 rpm). With an increase of the rotor speed to 3000 rpm the bubble size decreased, and the affected region became larger (**Fig. 3b**). Bubble buoyancy also decreased and with it the effect on surface instability. However, no bubbles were observed below the unit. As the rotor speed got closer to 4000 rpm (**Fig. 3c**) the bubble jet flow hit the wall of the tank and divided by following both upward and downward paths, the latter carrying the bubbles with it towards the region below the unit. Increasing the rotor speed to 5000 rpm enhanced the presence of the bottom dispersed bubbles towards the base of the water tank (**Fig. 3d**), thus promoting their full recirculation when they are captured again and re-dispersed into the high shear flow. Zuo et al. (2016) had reported in a previous analysis of the HSMC unit, in a similar water modelling setup, that a rotor speed of 6000 rpm is recommended for effectively dispersing the bubbles in full recirculation when the incoming Ar gas flow is set to 1 L/min^{-1}. Similarly, Kang et al. (2015) had reported on bubble dispersion in water by HSMC but using a lower gas flow rate of 0.3 L/min and found that this minimum rotor speed for reaching full bubble recirculating regime is in the range from 4000 to 5000 rpm, and that above 5000 rpm bubble size hardly decreases. It should be noted that bubbles can only survive in this recirculating motion if they are sufficiently small to stay suspended and the jet velocity is high enough for the dragging force of the downwards flow to overcome the natural bubble buoyancy towards the surface.

Scargiali et al. (2014) reported that the diameter, D, of each Ar bubble that is released from a tube is mainly determined by the gas flow rate, G, through the expression $D \alpha G^{1/3}$ and only weakly affected by

the nozzle diameter. Therefore, the lower the incoming flow rate, the smaller the initial bubbles to be dispersed. In the present study the gas flow of 1 L/min injected bubbles of about 15 mm (**Fig. 3a**), similarly reported by Zuo et al. (2016), and the gas flow of 0.1 L/min injected bubbles of approximately 6 mm diameter, as shown in **Fig. 3e-h**. In the same way, Kang et al (2015) reported injected bubbles of 10 mm diameter when using an inlet gas flow of 0.3 L/min. These previous studies on the HSMC unit also reported that the sharp decrease of the bubble size occurs more strongly for rotor speeds up to 3000 rpm, with almost no change for higher rotor speeds. Therefore, it was expected that a lower incoming gas flow rate would help to produce much smaller dispersed bubbles for the same rotor speed compared with a higher flow rate.

This can be appreciated in **Fig. 3e-h**, for a flow rate of 0.1 L/min, where the bubbles coming out of the tube and out of the stator holes were much smaller compared to the case of 1 L/min (**Fig. 3a-d**). The first consequence of this is that bubble buoyancy was much slower and the instabilities due to bubble rupture at surface were minimized at all rotor speeds. This is more clearly observed in the video recordings. Secondly, at same rotor speed of 2000rpm (**Fig. 3f**) the affected region by dispersed bubbles was larger in comparison with the one observed for the higher flow rate (**Fig. 3a**). This is because the water jets can carry the smaller bubbles further. Thirdly, the fine bubble jets reached the wall of the tank when the rotor speed was at around 2500 rpm (**Fig. 3g**), with consequently earlier presence of dispersed bubbles in most of the volume below the unit, and a clear full bubble recirculation could be observed when the rotor speed was 3000 rpm (**Fig. 3h**) and above.

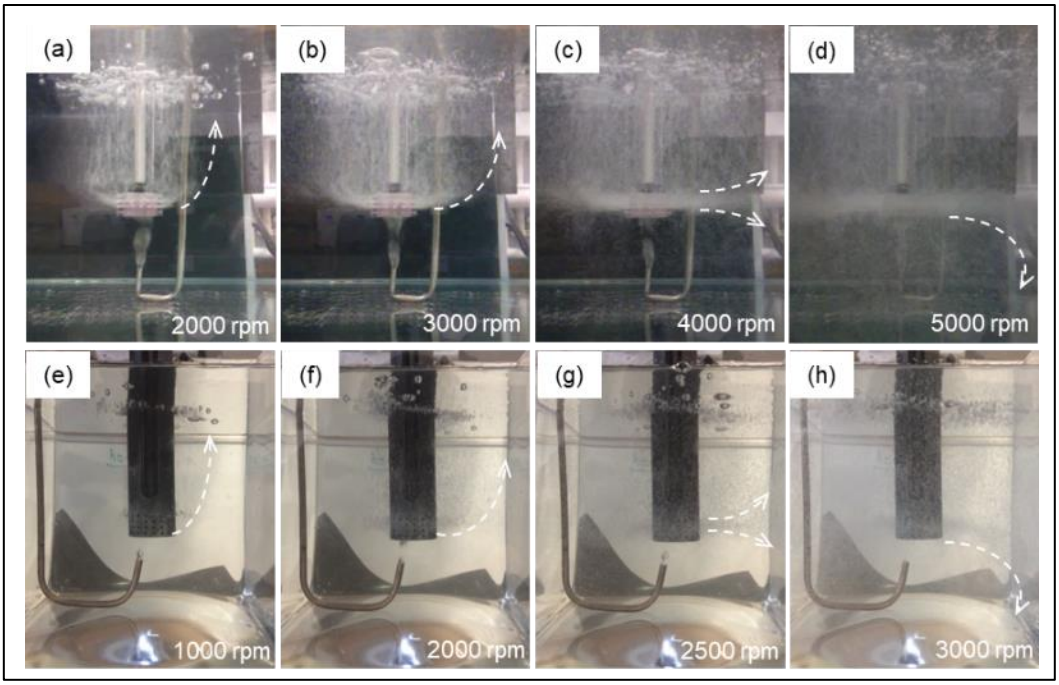

Fig. 3. Physical modelling of the HSMC degassing process in water, with variation of rotor speed and Ar gas flow rate. (a-d) 1 L/min (e-h) 0.1 L/min. Figure adapted from Lazaro-Nebreda et. al. (2018).

Fig. 4 gives the quantitative evaluation of the volume fraction of water in the tank showing presence of dispersed bubbles as a function of rotor speed for the two gas flow rates studied. Data from 0.3 L/min flow dispersion reported by Kang et. al. (2015) has been included for a better comparison of the results. A dashed line at 50% has been drawn to highlight the moment the bubble jets hit the wall. As the unit was immersed halfway inside the water tank, that point marks the transition from observing bubbles dispersed just above the stator holes and the beginning of the regime with dispersed jets both above and below the mixer enhancing the bubble recirculation flow. This line crosses with the 0.1 L/min curve at 2250 rpm, with the 0.3 L/min curve at 2750 rpm and it crosses at 3500 rpm for the case of the 1.0 L/min curve, thus highlighting the need of higher rotor speed to achieve the same bubble dispersion degree when increasing the gas flow rate.

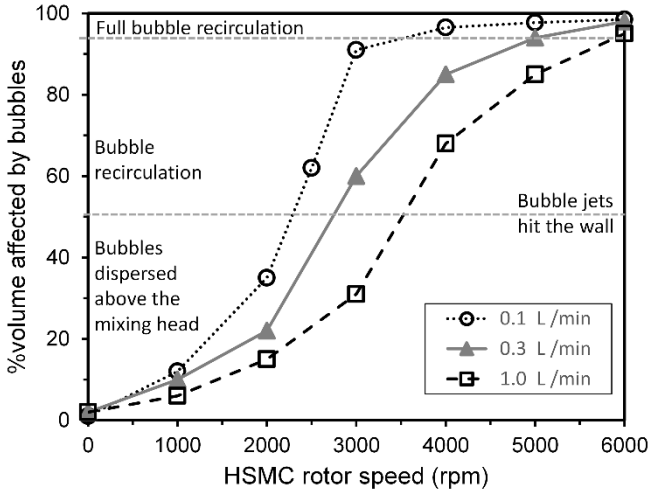

Fig. 4. Volume fraction of water affected by bubbles as a function of rotor speed and Ar flow rate. The 0.3 L/min line is reproduced from data in Kang et al. (2015)

A second dashed line has been drawn, at around 95%, to denote the moment that bubble recirculating flow reached the bottom of the tank below the HSMC unit. Further increase of the rotor speed caused no significant change on the volume affected by the dispersed bubbles, but rather finishing filling the corners of the tank. It can be appreciated how a minimum rotor speed of 6000rpm is required to reach this full bubble recirculation regime for a gas flow of 1 L/min, as also reported by Zuo et al. (2016). This minimum rotor speed decreases to 5000 rpm for a gas flow of 0.3 L/min, as reported by Kang et. al. (2015) and is only 3500 rpm in this study for the case of using 0.1 L/min gas flow.

This is a quite significant achievement for the high shear degassing technology as it means similar results in terms of bubble dispersion can be obtained by reducing both injected gas flow and rotor speed. The reduction of the inlet flow rate not only reduces process costs but also efficiency as it uses each injected bubble to its maximum effectiveness without losses due to bubble buoyancy. It also enhances the bubble size reduction and the bubble recirculation flow and with it the increased time they can remain in the fluid capturing dissolved gases before they reach the surface.

On the other hand, the power consumption of the HSMC unit can also be reduced. Hakanson (2018) described the power (P) transferred to the fluid by the rotor as $P = N_p \rho N^3 D^5$, where D is rotor diameter, N the rotor speed, ρ the fluid density and N_p the power number. According to Hakanson (2018) the N_p depends on mixer geometry but is constant with respect to rotor speed and diameter

under turbulent conditions, i.e. Re> 10^4, as in the case of this study. Therefore, power consumption is reduced by a factor of 5 when decreasing the minimum rotor speed from 6000 rpm to 3500 rpm and by a factor of 8 when using 3000 rpm instead of 6000 rpm.

It should be noted that these optimized parameters shown here are particular for the water/crucible tank dimensions selected for this study. However, if implemented in much larger crucibles, the earlier appearance of this bubble recirculation regime when using low gas flow rates, would give the HSMC technology a wider range for increasing the rotor speed without overpassing the unit working limits (<10000 rpm), something that would not be practical if using 1 L/min.

3.2. Effect of HSMC degassing on Hydrogen removal

Fig. 5 presents the evolution of the hydrogen concentration in the melt as a function of time for the three degassing methods used. The vertical dashed line marks the start of the holding stage after degassing (t = 10min). The horizontal dotted line gives the hydrogen equilibrium solubility level (0.056 $cm^3/100g$) in the solid alloy according to Tiryakioglu (2020). The horizontal dashed line gives the hydrogen (H) stabilisation (quasi-equilibrium) level (0.096 $cm^3/100g$) due to the relative humidity (RH) in the air in the laboratory the day of the experiment, as given by the expression H = 0.1772RH + 0.0394 provided by Eskin et al.(2015).

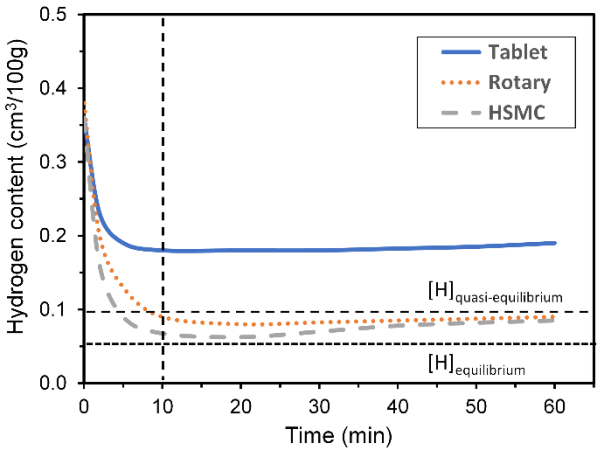

Fig. 5. Hydrogen concentration in the melt as a function of time for the three degassing methods. Degassing ends at t = 10 min. Sampling of tensile bars starts at t = 20 min.

All the melts started with a comparable hydrogen content (~ 0.37 ± 0.02 cm^3/100g), and the three methods all showed an initial high hydrogen reduction rate. Despite this, the tablet method quickly reached a steady value (~ 0.18 cm^3/100g) during the 5 minutes the bubbling lasted. It was clearly not effective at completely removing all possible hydrogen from melt as it was left far above the stabilization level. This is an expected result since industrial practice recommends either to do tablet degassing treatment in several steps or combined with rotary impeller to enhance the bubble distribution. When looking at the other two methods, both were effective at removing the hydrogen from the melts, reaching values below the quasi-equilibrium. Due to this they later show a slow but constant re-gassing towards the quasi-equilibrium level during the holding stage. In contrast, tablet degassing did not experience re-gassing as it did not reach that low level. It should be noted that re-gassing is a slow process and in the present study the melts did not exhibit clear re-gassing right after gas injection stopped but rather when the surface was skimmed off and disturbed for sampling the tensile bars.

In terms of degassing kinetics, the HSMC degassing was faster than rotary degassing, only requiring 5 minutes to reach the quasi-equilibrium level (0.096 cm^3/100g). With further HSMC degassing up to 10 minutes the hydrogen content decreased to 0.07 cm^3/100g, which is a very low level of hydrogen concentration. In comparison, the rotary degasser required 10 minutes to reach the quasi-equilibrium level. The hydrogen content evolution during the degassing process, H_t, can be described by Eq. 3, as shown by Warke et al. (2005), where H_{eq} denotes the equilibrium solubility level, H_0 the initial content, K_b the mass transfer coefficient at the melt/bubble interface, A_b the total interfacial area of the dispersed bubbles and V_m the volume of melt being processed.

$$H_t = H_{eq} + (H_0 - H_{eq}) \exp(-K_b A_b t/V_m) \quad (3)$$

Considering the experimental conditions, with similar H_0, H_{eq} and V_m in the three cases, and K_b independent of the degassing conditions, as reported by Warke et al. (2005), that leaves A_b as the key parameter to explain the differences observed in the hydrogen kinetics. Therefore, the higher removal rate with the HSMC degassing method highlights the much larger interfacial area of the bubbles dispersed in comparison with rotary degassing, even though the Ar gas flow used was 50 times lower.

As shown in **Fig. 3** and also reported by Kang et al. (2015) and Zuo et al. (2013), the bubbles dispersed by the HSMC technology can be reduced to sizes between 0.1-0.5 mm, which is much smaller

than the 10 mm bubble size that is usually obtained with the conventional rotary degassing process. For N bubbles of radius r, the total volume is V=4πr3N/3 and the total bubble surface area is A=4πr2N. Therefore, for a fixed volume of injected bubbles, the interfacial area of bubbles can be expressed by A=3V/r, i.e. is inverse proportional to the bubble size. Consequently, the interfacial area of the bubbles dispersed with the use of the HSMC technology is much larger, at least 20 to 100 times, than that obtained with conventional rotary degassers, explaining the faster diffusion rate of hydrogen into the bubbles during the degassing process, as shown in **Fig. 5**.

In terms of the required degassing processing time with the selected HSMC parameters, i.e. 0.1 L/min and 3000 rpm, the results are as expected when compared with previous studies of the HSMC degassing technology. Zuo et al (2013) initial tests of the HSMC technology in A356 molten aluminium alloy recommended processing times between 1 to 2 min when using a rotor speed of 6000 rpm and 1 L/min gas flow rate to fully degas a similar melt volume than the one used in this study. It is known, as described by Hakanson (2018), that the net flow rate passing through the stator holes is proportional to the rotor speed. For a fixed melt volume, a decrease in rotor speed from 6000rpm to 3000rpm would reduce to half the flow rate and double the time required for processing the melt through the unit. In that way, Dybalska et al. (2017) reported a processing time of 4 minutes when using a rotor speed of 3000 rpm to ensure effective particle dispersion in an alloy melt of similar volume, which is about double the time required by Zuo et al. (2013), and similar to the required time in the present study to lower the hydrogen content down to the quasi-equilibrium level.

After degassing, both rotary and HSMC degassed melts exhibit a quite stable but still decreasing hydrogen content during the initial 10 minutes, with final values of 0.08 cm^3/100g for rotary degassing and 0.06ml/100g for HSMC degassing. This further reduction is associated to the dispersed bubbles in the melt when the rotor stops. The remaining tiny bubbles require some time to reach the surface during which they join up with other bubbles on the way up. As HSMC bubbles are much smaller than rotary dispersed bubbles the resident time in the melt is higher and with it the chances to collect and carry more hydrogen out of the melt, explaining the final lower hydrogen content.

From the moment the melts were skimmed, and the sampling of the tensile bars was started, the disturbance of the protective surface oxide layer caused the hydrogen level to start increasing again (natural re-gassing). However, for the HSMC degassed melt, the levels remained lower, even after a

holding period of 50 minutes. This can be also explained by the remaining dispersed bubbles in the melt when degassing stops. The floating velocity, V_f, towards the surface can be expressed by the Stokes law as in Eq. 4, where g is the gravitational acceleration, ρ_{Ar} is the density of Ar, ρ_{melt} the density of the Al melt, ϕ the bubble diameter and η the melt viscosity.

$$V_f = g(\rho_{Ar} - \rho_{melt})\phi^2/(18\eta) \quad (4)$$

The floating speed decreases with reducing the bubble size and therefore the finer bubbles obtained by the HSMC unit and low gas flow rate can remain for longer in the melt. Not only they can continue capturing hydrogen for a longer period on their way towards the melt surface but can also hinder the re-gassing by preventing fresh hydrogen dissolving into the melt.

3.3. Effect of HSMC degassing on Density Index reduction

The results from density index evaluation during and after the degassing treatments are presented in **Fig. 6**. In this case the differences between degassing methods are clearer than by just using the hydrogen content assessment, especially during the holding stage. The density index values for the HSMC melt are significantly below the ones obtained for the other two degassing techniques. The tablet method always shows density index above 6%, highlighting its ineffectiveness at degassing. For rotary and HSMC techniques, the density index falls below the industrially accepted 3% value after the 10 minutes of degassing, although with HSMC values decreasing faster and towards lower final values, below 1%.

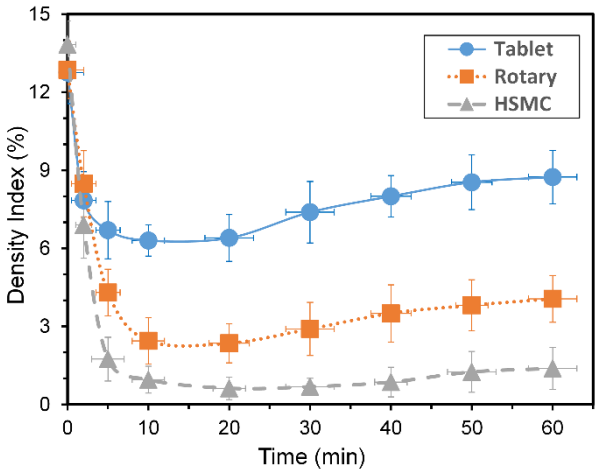

Fig. 6. Density index as a function of time during degassing and isothermal holding for the different degassing methods. Degassing ends at t = 10 min. Sampling of tensile bars starts at t = 20 min.

The differences between the methods are also clear during the isothermal holding stage in favour of the HSMC degassing. For the first 10 minutes after degassing the density index is quite constant in the three cases. Once tensile bars sampling started at t = 20 min, a significant increase in the density index was observed for the tablet and rotary degassed melts, while for the HSMC degassed melt the density index remained below 1.5% for up to 50 minutes after degassing and sampling. This slow re-gassing can be as well understood in terms of the small, dispersed bubbles left in the melt when the HSMC unit stops. These tiny bubbles not only keep collecting hydrogen on their way up, but also act as a kind of deep bed filtering system capturing the oxide particles or bi-films entrapped during sampling in the large bubble interfacial area and migrating them to the dross layer at the surface. Zuo et al. (2013) HSMC degassing study using a gas flow of 1 L/min and 6000 rpm rotor speed reported also reduced re-gassing during the holding stage but up to a maximum of 15 to 20 minutes after degassing, after which density index quickly started increasing way above the 3% limit. This previous result highlights again the importance of reducing the incoming gas flow rate to obtain even smaller and better dispersed bubbles with the HSMC degassing technology. This way they move slowly towards the surface (Eq.4), while offering a more complicated path for the oxide particles to pass through, thus enhancing their attachment to the bubble surface. In the present study with lower rotor speed and lower Ar gas flow, there was no re-gassing observed up to 50 minutes after HSMC degassing, which is a significant improvement for the HSMC technology. Similar low density index and minimal re-gassing for long holding periods when using low gas flow rate have been also reported by Lordan et al. (2019) on larger melts, highlighting the reproducibility of the HSMC degassing results. That way, and provided the surface is not intensively disturbed, the processed melt by the HSMC technology can rest for longer after degassing with the guarantee that neither hydrogen content nor density index will increase rapidly and will not require covering fluxes as it is common practice after rotary degassing.

3.4. Relationship between Density Index, Hydrogen content and RPT porosity

To better understand the results presented in the previous sections, a correlation graph between the hydrogen measurements (**Fig. 5**) and the calculated density index (**Fig. 6**) is given in **Fig. 7**. The data exhibit a good fit ($R^2 > 0.95$) to a quadratic function (included in the graph). Similar good correlations

were reported by Eskin et al. (2015) for the A356 and A380 aluminium alloys. Owing to the well-known difficulty of accurately measuring the hydrogen content in aluminium alloy melts in industry, this correlation reinforces the possibility of assessing the hydrogen levels in the melts indirectly via the RPT sampling as it is commonly done in industry.

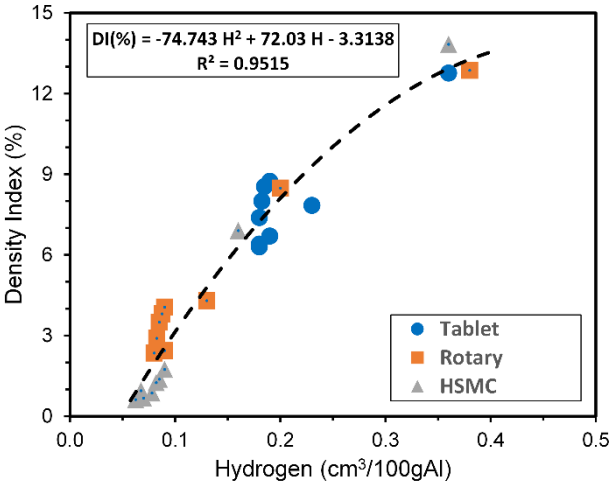

Fig. 7. Correlation between density index (DI) and hydrogen (H) content in the melt for the three degassing methods used in this study.

However, despite this good correlation it should not be forgotten that the measurement of density index considers more than just the hydrogen content and that is another reason for its extended use in industry. As Dispinar and Campbell (2004) described, the density index refers to the potential porosity to be originated in the castings and therefore depends not only on the hydrogen content necessary for the pore expansion but also very sensitively the oxide bi-film content that initiate the pores. This can be well appreciated in **Fig. 7**. For the tablet-degassed melt the hydrogen content remains almost constant, but the density index ranges between 6% and 9%. On the other hand, when the hydrogen level is below 0.1 $cm^3/100g$, i.e. the density index for rotary degassed melt varies from 2.3% to 4.5%, while for the HSMC degassed melt it varies only between 0.62% and 1.74%. Therefore, the rotary degassed melt density index values are much higher and scattered than obtained after HSMC degassing. This variability in the density index regardless of the hydrogen was also reported by Dispinar et al. (2010) and is caused by the dissimilar oxide bi-film content in the melts after degassing and the way each method deals with the

oxide bi-film removal. To better understand this, **Fig. 8** shows the vertically sectioned RPT samples solidified under partial vacuum at different times during degassing for the rotary and HSMC degassing methods, which help visualizing the differences in the melt processing. **Fig. 9** presents the pore size distributions for the RPT samples shown in **Fig. 8** and **Table 1** gives the average and maximum pore length in each case, as well as the density of pores, which is an indicator of the size and level of bi-films present in the melt, as reported by Dispinar and Campbell (2004). In addition, **Fig. 10** presents the micrographs of the dross skimmed off after degassing and prior sampling by the rotary and HSMC degassing methods, which show the type of oxides that are being removed from the melt in each case.

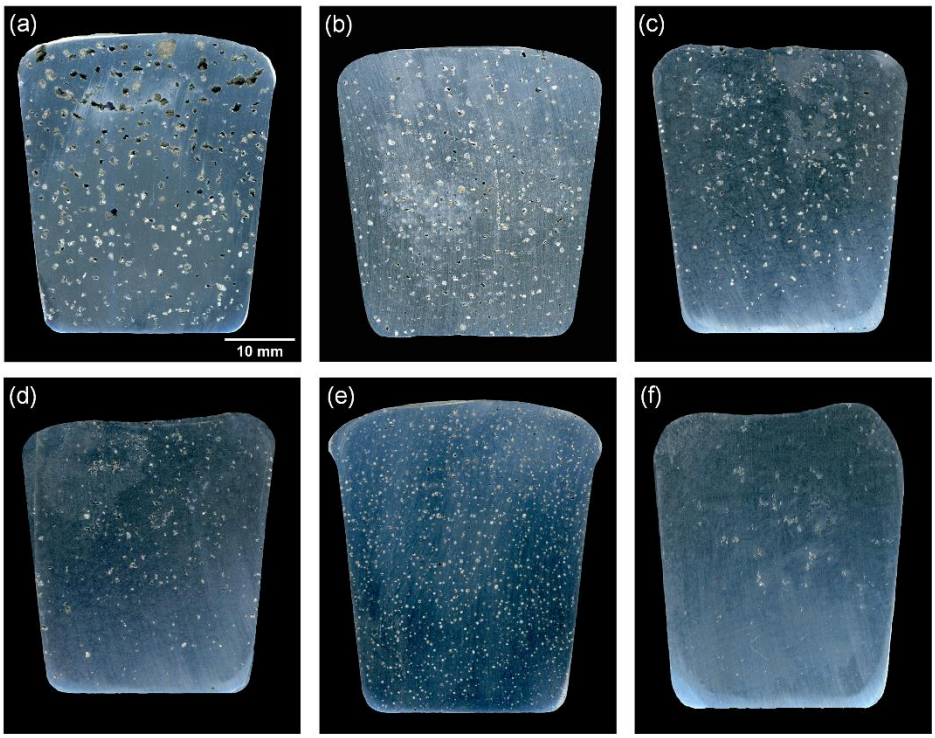

Fig. 8. Porosity in the RPT samples solidified under partial vacuum. (a) before degassing; and during degassing: (b) rotary, 2 min; (c) rotary, 5 min; (d) rotary, 10 min; (e) HSMC, 2 min; (f) HSMC, 5 min.

Before degassing, the RPT sample solidified under partial vacuum (**Fig. 8a**) exhibits the typical convex top surface caused by expansion due to porosity formation during solidification. The large pores follow a bimodal size distribution, with peaks at around 420 μm and 850 μm and an average pore size of 652 μm. The maximum pore size is 1200 μm and the pore density is 37 pores/cm^2. With the application of Rotary degassing the top surface of the RPT samples transforms from convex to concave shape as processing

time increases (**Fig. 8b-d**), because of the removal of hydrogen and oxide bi-films that promote the porosity expansion during solidification. Pore density decreases fast towards almost half of the initial value in 5 minutes and the pore size distribution moves towards lower values, acquiring a unimodal shape. This highlights that the larger bi-films are removed from the melt faster than the smaller ones by the rotary degassing method, something that agrees with previous findings by Warke et al. (2005). The removal of the smaller oxides requires of longer processing times. However, it can be appreciated that there is not much difference in the results from 5 min to 10 min of processing. As it can be observed in **Fig. 10a,** the dross collected after rotary degassing consists mostly of large poorly wetted bi-films, those that are more easily lifted to the surface by the large bubbles. This suggests that further rotary degassing is not fully effective at removing the smaller bi-films from the melt but only removing the dissolved hydrogen in the melt, as shown in **Fig. 3**. This causes the small natural reabsorption of hydrogen during the holding stage to produce the significant increase and variability in the DI% values, as mentioned before.

On the other hand, when the HSMC degassing is applied to the melt, it can be observed how during the first 2 minutes of processing (**Fig. 8e**) the number density of pores increases up to 97cm^{-2}, almost 3 times the initial level, but the pore length decreases significantly, to almost one third of the initial size. The reason for that is that the HSMC degassing is not only dispersing the tiny bubbles in the melt but also dispersing the large poorly wetted oxide bi-films into smaller and better wetted bi-films with less potency to form large pores during solidification. With further HSMC processing up to 5 minutes (**Fig. 8f**) the small oxide bi-films are further dispersed, resulting in even smaller pores in the RPT samples. HSMC processing up to 10 minutes continues dispersing the oxide bi-films, resulting in reduced porosity size in RPT samples solidified under vacuum during degassing, although the effect is less significant as the pore size distribution or the density of pores do not vary much when compared with HSMC for 5 minutes. This suggests that an increase in HSMC processing above 10 minutes for the selected melt quantity might not translate in further improvement of the melt quality. **Fig. 10b** shows how the dross collected after HSMC degassing consists of fragmented and better wetted oxide films rather than the typical large bi-film layer. The poorly wetted surface inside the bi-film is therefore reduced with the use of HSMC, and the films eventually transformed into individual and well wetted particles, which are more easily captured and lifted to the surface by the small bubbles that the HSMC technology provides. In

consequence, it is difficult for the particles to act as initiators for the porosity during solidification, regardless of the hydrogen content, explaining the sharp decrease in density of pores and the reduced variability in the density index.

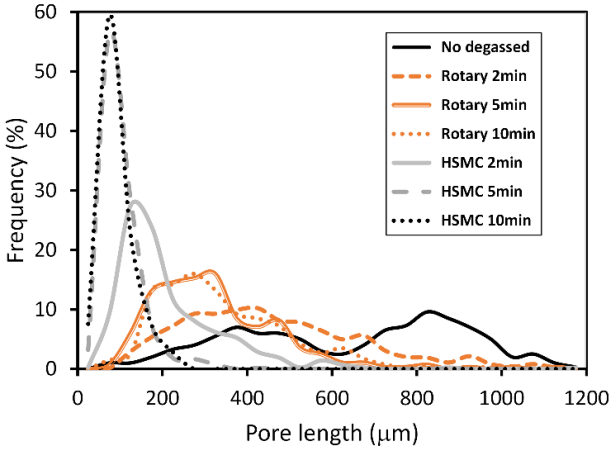

Fig. 9. Pore size distribution of the RPT samples solidified under vacuum during degassing.

Table 1
Porosity analysis on the RPT samples solidified under vacuum during degassing.

	Average pore size (μm)	Max. pore size (μm)	pores/cm^2
Before degassing *	652	1200	37
Rotary 2 min	474	1075	35
Rotary 5 min	328	825	24
Rotary 10 min	339	800	22
HSMC 2 min	213	625	94
HSMC 5 min	103	375	13
HSMC 10 min	94	250	11

*Bimodal distribution

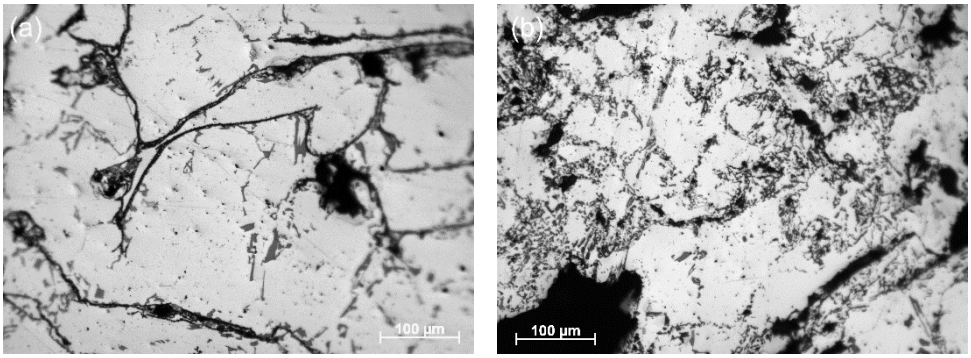

Fig. 10. Micrographs of the dross collected after melt treatment by (a) rotary and (b) HSMC degassing.

3.5. Effect of HSMC degassing on casting integrity before tensile testing

Representative microstructures of the as-cast tensile specimens, at 10 minutes after degassing, are given in **Fig. 11** for the three degassing methods considered in this study. The tensile bars exhibited similar microstructural features in terms of dendritic arm spacing, size and distribution of secondary phases, which was expected as all samples were cast under similar cooling conditions. The only difference between the three degassing methods was the different levels of porosity. In the sample solidified after tablet degassing (**Fig. 11a**) pores larger than 100 μm can be seen, whereas for the sample obtained after rotary degassing (**Fig. 11b**) the pores observed are in the range from 50 to 100 μm. On the other hand, the sample obtained after HSMC degassing (**Fig. 11c**) showed pores with size below 10 μm. With increasing holding time after degassing, no changes in microstructure were observed between the degassing methods but the tablet and rotary degassed samples exhibited higher defect content while the HSMC tensile bars kept a low porosity level. Similar findings were reported by Uludag et al. (2018), and are caused by the higher presence of bi-films in the melts and their expansion due to the gradual reabsorption of hydrogen during re-gassing.

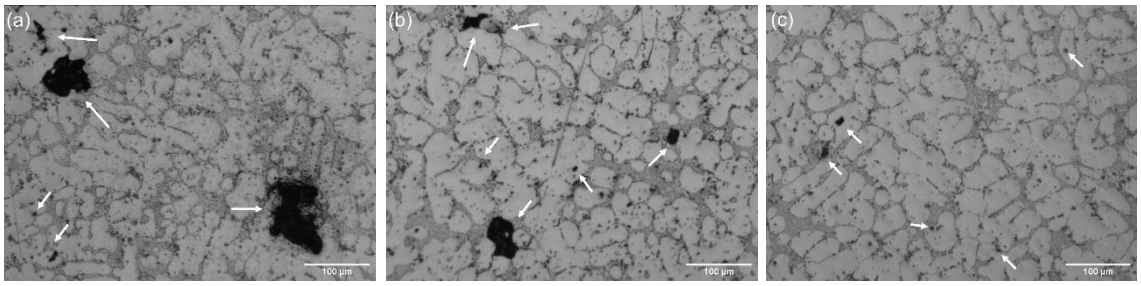

Fig. 11. Representative microstructure of the tensile bars before testing for each degassing method. Samples obtained at 10 min after degassing. (a) tablet; (b) rotary and (c) HSMC degassing.

3.6. Effect of HSMC degassing on tensile properties

The tensile properties of the tensile bars cast at different holding times after each degassing method are shown in **Fig. 12**. Each point and error bars correspond to the average and standard deviation of the results obtained from the 4 specimens cast at each condition.

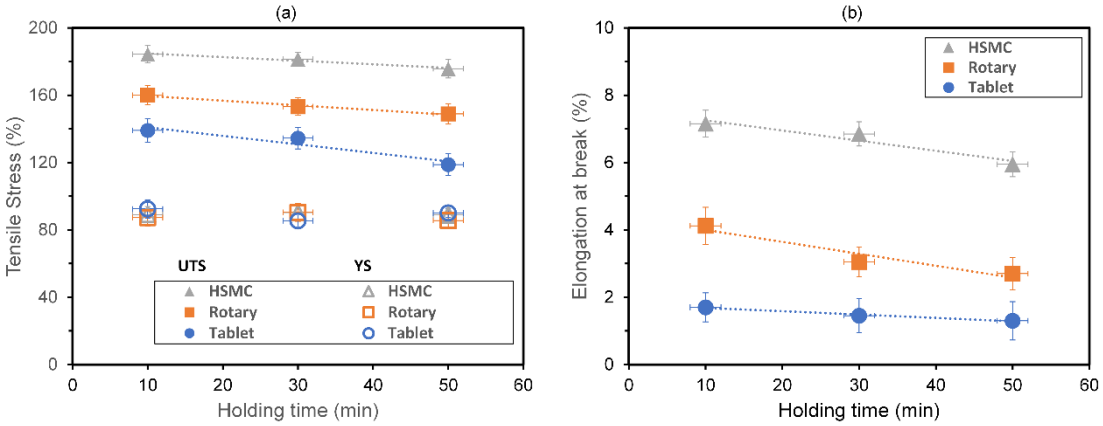

Fig. 12. Tensile properties of the tensile specimens as a function of holding time after degassing. (a) yield strength (YS) and ultimate tensile strength (UTS) and (b) elongation at break.

The yield strength was unaffected by either the degassing method or the holding time after degassing (**Fig. 12a**), with average values of 89.3 ± 4.1 MPa, 87.8 ± 5.1 MPa and 89.5 ± 3.9 MPa for tablet, rotary and HSMC degassing, respectively. Significant difference is observed, however, in the ultimate tensile strength (**Fig. 12a**) and in the elongation at fracture (**Fig. 12b**), with HSMC degassed specimens showing the best performance with average values for UTS and elongation of 178.8 ± 6.9 MPa and 6.7 ± 0.6%, respectively. Rotary degassed bars show average properties of 154.1 ± 7.1 MPa and 3.3 ± 0.8%, similar to Akthar et al. (2009). The tablet degassed bars showed the worst results with average values of 130.8 ± 10.3 MPa and 1.5 ± 0.4 %.

A linear decrease of UTS and elongation with holding time is observed in all three cases (trend dashed lines and linear fitting included in the plots for better visualization). The UTS decay is at 0.51 MPa/min for the tablet degassed bars and 0.28 MPa/min for rotary degassing. It is only 0.19 MPa/min for HSMC degassed specimens, which represents a reduction of 63% compared to tablet degassing and 32% reduction compared to rotary degassing. For the elongation, the decay is minimal for tablet degassed samples, which is somehow expected considering the initial low values. For rotary degassed samples the elongation decays at 0.035 %/min, while for HSMC samples this decay is only 0.025 %/min (29% less).

The tensile properties of Al-Si alloys are known to be dependent on multiple factors such as the grain size and structure, the size and distribution of secondary phases and the size and distribution of defects.

As reported by Uludag et al. (2018) the microstructure does not vary during the holding stage, if casting conditions are maintained, but the amount of porosity tends to increase affecting the mechanical properties, as shown here in **Fig. 12**. The reason is the remaining oxide bi-films in the melt after degassing and their expansion during the solidification is enhanced by the hydrogen reabsorption during holding stage. Wang et al. (2013) reported that the employment of an in-furnace filter had a very positive effect on reducing inclusions and oxide bi-films, therefore decreasing casting porosity and improving the tensile properties in the test bars. They reported values of elongation (El) from El < 4.5% before filtering to El > 6% after filtering. The results of the present study show similar improvement, therefore confirming the enhanced elimination of oxide bi-films by using the HSMC degassing technology.

3.7. Effect of HSMC degassing on fracture surface

The fracture surfaces of the tested tensile bars cast at 10 minutes after degassing are given in **Fig. 13a-c**. The vertical sections of the tensile bars at fracture locations are given in **Fig. 13d-f**, highlighting the differences in defect content between the different degassing methods. The observation of the fracture surfaces via SEM is given in **Fig. 14.** Two types of defects were clearly identified at the fractured surface of the tensile bars after tablet degassing (**Fig. 13a** and **Fig. 14a**). One is the rounded voids, identified as gas porosity, and the other is the rough brighter areas, identified as oxide defects (see **Table 2**). Both cover most of the fracture surface area, which exhibits a high degree of tortuosity. For the bars after rotary degassing (**Fig. 13b** and **Fig. 14b**) the surface roughness remains relatively high but the number of defects at the surface decreases significantly, especially the gas porosity. However, the surface area still exhibits a high degree of oxide defects. On the contrary, for the bars after HSMC degassing (**Fig. 13c** and **Fig. 14c**) the fracture surface is smooth, with no visible gas porosity and smaller oxide defects.

Table 2
Results of EDS analysis on the rough brighter areas of the fracture surfaces.

Element	Weight %	Atomic %	Error %
O	19.27	28.82	10.33
Mg	5.21	5.13	5.29
Al	48.75	43.24	3.43
Si	26.77	22.81	6.84

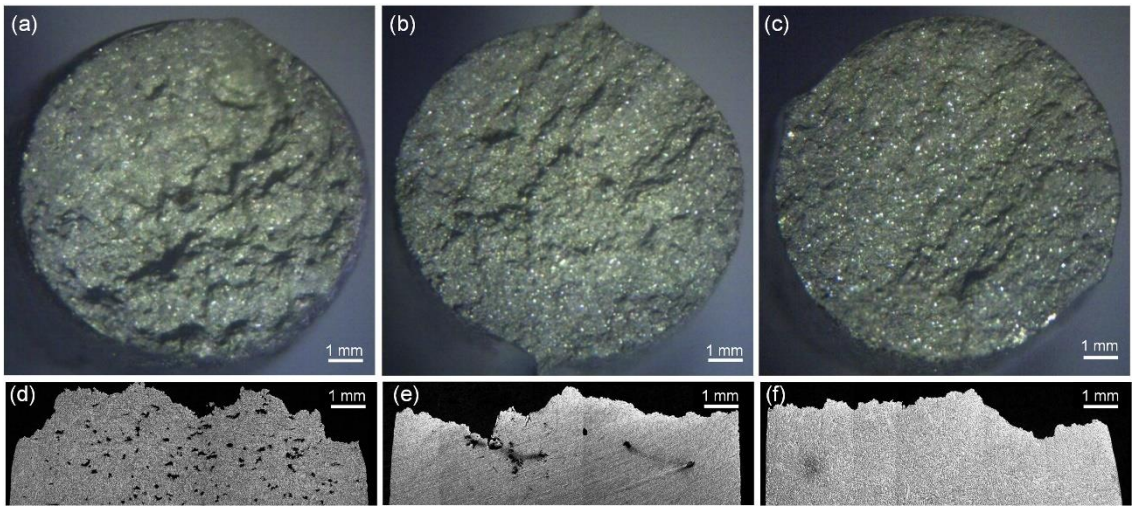

Fig. 13. Fracture surfaces of the post-mortem tensile bars cast at 10min after degassing. (a) tablet degassing; (b) rotary degassing; (c) HSMC degassing. (d-f) Vertical sections of samples in (a-c).

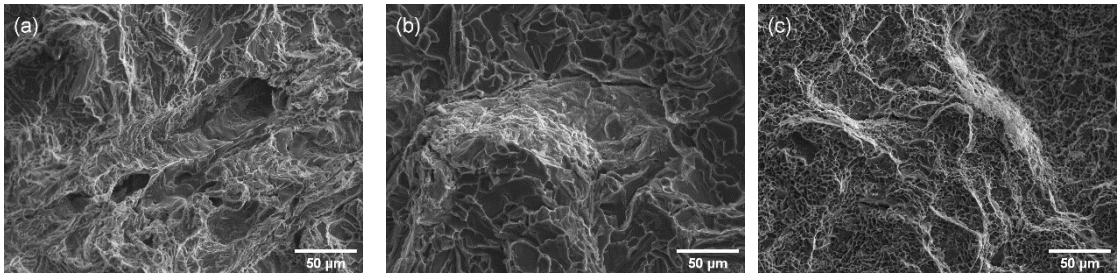

Fig. 14. SEM micrographs showing the oxide films on the fracture surface of the tensile specimens. (a) tablet degassing; (b) rotary degassing; (c) HSMC degassing.

The evolution of the area fraction of defects at the fracture surface during the holding time for the three degassing methods is given in **Fig. 15**. It can be clearly appreciated how the tensile bars after HSMC exhibit very low and constant level of defects, explaining the good performance in the tensile properties. On the other hand, the tensile bars after tablet and rotary degassing show a constant increase of the fraction of defects at the fracture surface, explaining the gradual decay of the tensile properties.

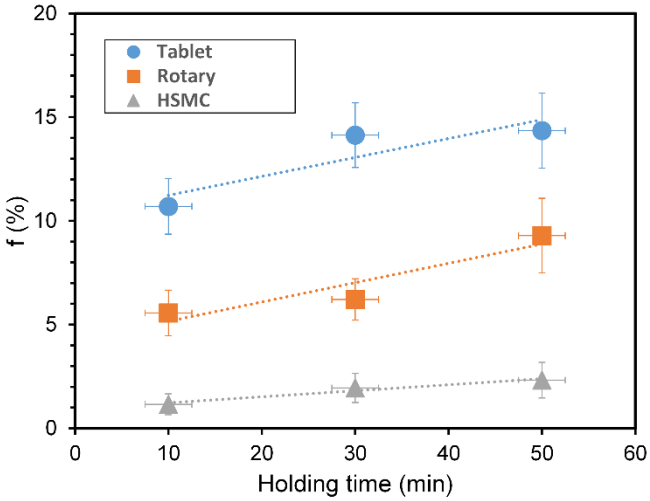

Fig. 15. Area fraction of defects at fracture surface (f) as a function of holding time after degassing.

A good correlation between tensile properties and the measured fraction of porosity at the fracture surface in the tensile bars is given in **Fig. 16**. Similar findings were reported and discussed by Caceres and Selling (1996) and more recently by Lordan et al. (2020), highlighting the importance of good melt quality to produce castings with low amount of defects.

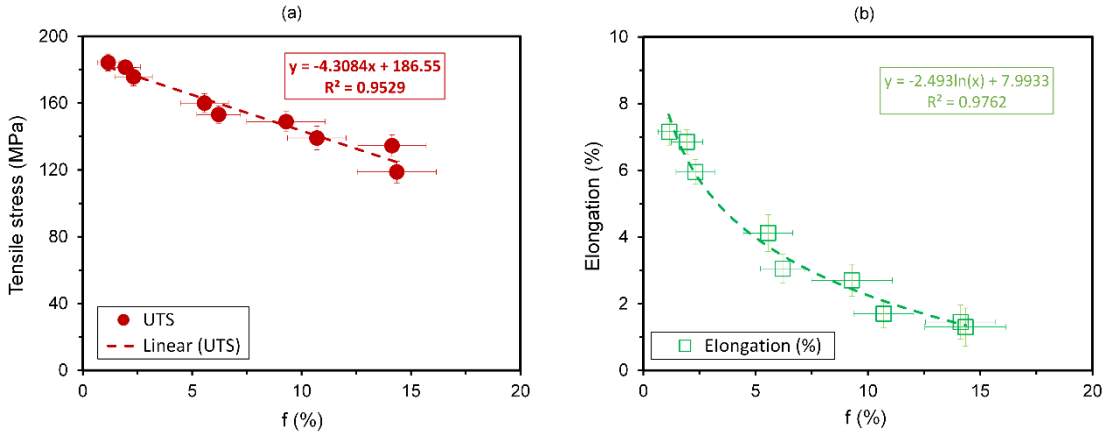

Fig. 16. Tensile properties as a function of the fraction of defects at fracture surface for (a) UTS; (b) Elongation.

4. Conclusions

The innovative HSMC degassing technology developed at BCAST has been investigated by water modelling and improved by determining the required gas flow and rotor speed for an efficient bubble

dispersion. The key finding is that when very low gas flow is used, lower rotor speed is needed to achieve an effective bubble dispersion. This has clear benefits in terms of reduced processing costs and increased process efficiency. The improved HSMC degassing parameters have been applied to aluminium melts and the results compared with conventional degassing methods showing better and faster removal of hydrogen and oxide bi-films. Rotary degassing is effective at removing hydrogen from the melt, but it is not for removing oxide bi-films. The HSMC degassing technology can effectively remove both the hydrogen and the entrapped oxide bi-films at the same time because it can operate at higher speeds without causing surface turbulences. This significantly improves the melt quality and maintains it for longer after degassing. Consequently, the aluminium melt processed by the HSMC degassing technology does not need of covering fluxes, as it is commonly required after rotary degassing. Castings produced with HSMC degassed melts exhibit very low level of porosity and significantly improved tensile properties, even after holding the melt for up to 60 minutes. The HSMC degassing process could be easily implemented in industry by replacing the current rotary impeller technique with minimal impact on the casting process but with all the benefits of improved melt quality at reduced cost.

CRediT authorship contribution statement

Jaime Lazaro-Nebreda: Methodology, Investigation, Validation, Formal analysis, Writing - original draft, Visualization. **Jayesh B. Patel:** Conceptualization, Investigation, Resources, Writing - review & editing, Visualization, Supervision. **Zhongyun Fan:** Writing - review & editing, Supervision, Funding acquisition.

Declaration of Competing Interest

The authors declare that they have no known competing financial interests or personal relationships that could have appeared to influence the work reported in this paper.

Acknowledgements

The financial support from EPSRC (UK) under grant number EP/N007638/1 of the Future Liquid Metal Engineering Hub is gratefully acknowledged. The high shear degassing work initiated by Dr. Yubo Zuo is also thankfully appreciated.

References

Akhtar, S., Dispinar, D., Arnberg, L., Di Sabatino, M., 2009. Effect of hydrogen content, melt cleanliness and solidification conditions on tensile properties of A356 alloy. International Journal of Cast Metals Research 22, 22-25. https://doi.org/10.1179/136404609X367245

Ammar, H.R, Samuel A.M., Samuel, F.H., 2008. Porosity and the fatigue behaviour of hypoeutectic and hypereutectic aluminum-silicon casting alloy. International Journal of Fatigue 30(6), 1024-1035. https://doi.org/10.1016/j.ijfatigue.2007.08.012

ASTM B108 / B108M-19, Standard Specification for Aluminum-Alloy Permanent Mold Castings. Annual book of ASTM standards, vol 02.02. West Conshohocken, PA, ASTM International; 2019. http://www.astm.org/cgi-bin/resolver.cgi?B108B108M

ASTM E8-03, Standard Test Methods for Tension Testing of Metallic Materials, ASTM International, West Conshohocken, PA, 2003. http://www.astm.org/cgi-bin/resolver.cgi?E8

Cáceres, C.H., Selling, B.I., 1996. Casting defects and the tensile properties of an Al-Si-Mg alloy. Materials Science and Engineering A 220, 109116. https://doi.org/10.1016/S0921-5093(96)10433-0

Camacho-Martínez, J.L., Ramírez-Argáez, M.A., Zenit-Camacho, R., Juárez-Hernández, A., Barceinas-Sánchez, J.D.O., Trápaga-Martínez, G., 2010. Physical Modelling of an Aluminium Degassing Operation with Rotating Impellers—A Comparative Hydrodynamic Analysis. Materials and Manufacturing Processes 25(7), 581-591. https://doi.org/10.1080/10426910903367386

Camacho-Martínez, J.L, Ramírez-Argáez, M., Juárez-Hernández, A., González-Rivera, C., Trápaga-Martínez G., 2012**.** Novel Degasification Design for Aluminum Using an Impeller Degasification Water Physical Model. Materials and Manufacturing Processes 27(5), 556-560. https://doi.org/10.1080/10426914.2011.593234

Campbell, J. 'Castings', 2nd ed.; 2003, Oxford, Butterworth-Heinemann

Chaijaruwanich, A., Dashwood, R. J., Lee, P. D., & Nagaumi, H., 2006. Pore evolution in a direct chill cast Al-6 wt.% Mg alloy during hot rolling. Acta Materialia 54(19), 5185-5194. https://doi.org/10.1016/j.actamat.2006.06.029

Dispinar, D., Akhtar, S., Nordmark, A., Di Sabatino, M., Arnberg, L., 2010. Degassing, hydrogen and porosity phenomena in A356. Materials Science and Engineering A 527, 3719-3725. https://doi.org/10.1016/j.msea.2010.01.088

Dispinar, D., Campbell, J., 2004. Critical assessment of reduced pressure test. Part 1: Porosity phenomena. International Journal of Cast Metals Research 17(5), 280-286. 10.1179/136404604225020696

Dong, X., Zhang, Y., Amirkhanlou, S., Ji, S., 2018. High performance gravity cast Al9Si0.45Mg0.4Cu alloy inoculated with AlB2 and TiB2. Journal of Materials Processing Technology 252, 604-611. http://dx.doi.org/10.1016/j.jmatprotec.2017.10.028

Dybalska, A., Eskin, D., Patel, J.B., 2017. Evaluation of Shearing Time Sufficient for Effective Liquid Metal Processing. JOM 69, 720–724. https://doi.org/10.1007/s11837-017-2286-x

Eskin, D., Alba-Baena, N., Pabel, T., da Silva, M., 2015. Ultrasonic degassing of aluminium alloys: basic studies and practical implementation. Materials Science and Technology 31(1), 79-84. https://doi.org/10.1179/1743284714Y.0000000587

Fan, Z., Wang, Y., Xia, M., Arumuganathar, S., 2009. Enhanced heterogeneous nucleation in AZ91D alloy by intensive melt shearing. Acta Materialia 57(16), 4891-4901. https://doi.org/10.1016/j.actamat.2009.06.052

Fan, Z., Zuo, Y.B., Jiang, B., 2011. A New Technology for Treating Liquid Metals with Intensive Melt Shearing. Materials Science Forum 690, 141–144. https://doi.org/10.4028/www.scientific.net/msf.690.141

Gyarmati, G., Fegyverneki, G., Tokár, M., Mende, T., 2020. The Effects of Rotary Degassing Treatments on the Melt Quality of an Al–Si Casting Alloy. International Journal of Metalcasting. https://doi.org/10.1007/s40962-020-00428-z

Hakansson, A., 2018. Rotor-Stator mixers: From batch to continuous mode of operation-A review. Processes 6(4), 32. https://doi.org/10.3390/pr6040032

Hernández-Hernández, M., Camacho-Martínez, J.L., González-Rivera, C., Ramírez-Argáez, M.A., 2016. Impeller design assisted by physical modeling and pilot plant trials. Journal of Materials Processing Technology 236, 1-8. https://doi.org/10.1016/j.jmatprotec.2016.04.031

Hernández-Hernández, M., Cruz-Mendez, W., González-Rivera, C., Ramírez-Argáez, M.A., 2015. Effect of Process Variables on Kinetics and Gas Consumption in Rotor-Degassing Assisted by Physical and Mathematical Modeling. Materials and Manufacturing Processes 30(2), 216-221. https://doi.org/10.1080/10426914.2014.952303

Lazaro-Nebreda, J., Patel, J.B, Scamans, G., Fan, Z., 2018. Multi-purpose high shear melt conditioning technology for effective melt quality and for recycling of Al-alloy scrap. Proceedings of the 16th International Aluminium Alloys Conference (ICAA16), 17-21 June, Montreal, Canada, pp. 401623. http://www.icaa-conference.net/ICAA16/Papers/Sustainability/401623%20Lazaro-Nebreda_final.pdf

Kang, Y.Y., Lin, Y., Liu, X.D., Sun, C., Yuan, S.S., Zuo, Y.B., Cui, J.Z., 2015. Study on the High Shear Degassing Process with Water Simulation. Advanced Materials Research 1120–1121, 1214–1219. https://doi.org/10.4028/www.scientific.net/amr.1120-1121.1214

Lordan, E., Lazaro-Nebreda, J., Zhang, Y., Duo, K., Blake, P., Fan, Z., 2020. On the relationship between internal porosity and the tensile ductility of aluminium alloy die-castings. Materials Science and Engineering A 778, 139107. https://doi.org/10.1016/j.msea.2020.139107

Lordan, E., Lazaro-Nebreda, J., Zhang, Y., Fan, Z., 2019. Effective Degassing for Reduced Variability in High-Pressure Die Casting Performance. JOM 71**,** 824–830. https://doi.org/10.1007/s11837-018-3186-4

Mostafaei, M., Ghobadi, M., Eisaabadi B., G., Uludag, M., Tiryakioglu, M., 2016. Evaluation of the Effects of Rotary Degassing Process Variables on the Quality of A357 Aluminum Alloy Castings. Metallurgical and Materials Transactions B 47, 3469–3475. https://doi.org/10.1007/s11663-016-0786-7

Polmear, I. J., 1995. Light Alloys: Metallurgy of the Light Metals (3rd ed.). Virginia University: Wiley.

Scargiali, F., Busciglio, A., Grisafi, F. Brucato, A., 2014. Bubble formation at variously inclined nozzles. Chemical Engineering & Technology 37(9), 1507-1514. https://doi.org/10.1002/ceat.201300511

Tan, E., Tarakcilar, A., Dispinar, D., Colak, M., Kayikci, R., 2011. Reproducibility of Reduced Pressure Test Results in Testing of Liquid Aluminum Gas Levels. Proceedings of the 6th International Advanced Technologies Symposium (IATS11), 16-18 May, Elazig, Turkey, pp. 321-324

Tiryakioglu, M., 2020. The effect of hydrogen on pore formation in aluminum alloy castings: Myth versus reality. Metals 10(3), 368. https://doi.org/10.3390/met10030368

Tzanakis, I., Lebon, G.S.B., Eskin, D.G., Pericleous, K.A., 2017. Characterizing the cavitation development and acoustic spectrum in various liquids. Ultrasonics Sonochemistry 34, 651-662. https://doi.org/10.1016/j.ultsonch.2016.06.034

Uludag, M., Cetin, R., Gemi, L., Dispinar, D., 2018. Change in porosity of A356 by holding time and its effect on the mechanical properties. Journal of Materials Engineering and Performance 27, 5141-5151. https://doi.org/10.1007/s11665-018-3534-0

Wan, B., Chen, W., Mao, M., Fu, Z., Zhu, D., 2018. Numerical simulation of a stirring purifying technology for aluminum melt. Journal of Materials Processing Technology. 251, 330–342. https://doi.org/10.1016/j.jmatprotec.2017.09.001

Wang, Y., Neff, D., Schwam, D., Zhu, X., Chen, C., 2013. Optimization of permanent mold mechanical property test bars in A356 alloy using a new mold design. International Journal of Metalcasting 7, 25-38. https://doi.org/10.1007/BF03355556

Warke, V.S., Shankar, S., Makhlouf, M.M., 2005a. Mathematical modelling and computer simulation of molten aluminum cleansing by the rotating impeller degasser: Part I. Fluid flow. Journal of Materials Processing Technology 168(1), 112–118. https://doi.org/10.1016/j.jmatprotec.2004.10.017

Warke, V.S., Shankar, S., Makhlouf, M.M., 2005b. Mathematical modelling and computer simulation of molten aluminum cleansing by the rotating impeller degasser: Part II. Removal of hydrogen gas and solid particles. Journal of Materials Processing Technology 168(1), 119–126. https://doi.org/10.1016/j.jmatprotec.2004.10.016

Yamamoto, T., Kato, K., Komarov, S. V., Ueno, Y., Hayashi, M., & Ishiwata, Y., 2018. Investigation of melt stirring in aluminum melting furnace through Water model. Journal of Materials Processing Technology 259, 409–415. https://doi.org/10.1016/j.jmatprotec.2018.04.025

Zhang, L., Lv, X., Torgerson, A.T., Long, M., 2011. Removal of Impurity Elements from Molten Aluminum: A Review. Mineral Processing and Extractive Metallurgy Review, 32(3), 150-228. https://doi.org/10.1080/08827508.2010.483396

Zhang, Y., Lordan, E., Duo, K., Wang, S., Fan, Z., 2020. Influence of porosity characteristics on the variability in mechanical properties of high pressure die casting (HPDC) AlSi7MgMn alloys. Journal of Manufacturing Processes 56A, 500-509. https://doi.org/10.1016/j.jmapro.2020.04.071

Zhang, Y., Patel, J.B., Lazaro-Nebreda, J., Fan, Z., 2018. Improved Defect Control and Mechanical Property Variation in High-Pressure Die Casting of A380 Alloy by High Shear Melt Conditioning. JOM 70, 2726–2730. https://doi.org/10.1007/s11837-018-3005-y

Zuo, Y.B., Jiang, B., Zhang, Y., Fan, Z., 2013. Degassing LM25 aluminium alloy by novel degassing technology with intensive melt shearing. International Journal of Cast Metals Research 26(1), 16-21. https://doi.org/10.1179/1743133612Y.0000000019

Zuo, Y.B., Kang, Y.Y, Lin, Y., Liu, X., Sun, C., Yuan, S. Cui, J., 2015. A new high shear degassing technology and mechanism for 7032 alloy. China Foundry 12, 293-298.

Zuo, Y.B, Kang, Y.Y, Lin, Y., Zhu, Q.F., Li, L., Li, Z.Z., Cui, J.Z., 2016. Dispersion behaviour of Ar bubbles under intensive shearing and its effect on degassing effect of 7075 alloy. The Chinese Journal of Nonferrous Metals 26(3), 486-493. https://caod.oriprobe.com/articles/48132534/Dispersion_behaviour_of_Ar_bubbles_under_intensive.htm

Zuo Y.B., Lin Y., Kang Y.Y., Cui, J.Z., 2016. Effects of Rotor Rotation Speed and Gas Flow Rate on the Degassing Efficiency of 2524 Aluminum Alloy in Rotary Degassing Process. Journal of Northeastern

University Natural Science 37(5), 653-657. http://xuebao.neu.edu.cn/natural/EN/10.12068/j.issn.1005-3026.2016.05.010

Zuo, Y., Jiang, B., Enright, P., Scamans, G.M., Fan, F., 2011. Degassing of LM24 Al alloy by intensive melt shearing. International Journal of Cast Metals Research 24, 307-313. https://doi.org/10.1179/1743133611Y.0000000002

Figure captions

Fig. 1. Schematic of the rotor-stator HSMC unit. (a) lateral and bottom view, (b) inside a melt illustrating the degassing procedure.

Fig. 2. (a) Geometry of the standard ´Stahl´ mould used to produce tensile specimens according to ASTM B108 (arrows indicate the nominal flow of the liquid metal); (b) tensile specimen geometry and dimensions (dotted line indicate region for pre-test microstructure evaluation). Dimensions in mm.

Fig. 3. Physical modelling of the HSMC degassing process in water, with variation of rotor speed and Ar gas flow rate. (a-d) 1 L/min (e-h) 0.1 L/min. Figure adapted from Lazaro-Nebreda et. al. (2018).

Fig. 4. Volume fraction of water affected by bubbles as a function of rotor speed and Ar flow rate. The 0.3 L/min line is reproduced from data in Kang et al. (2015)

Fig. 5. Hydrogen concentration in the melt as a function of time for the three degassing methods. Degassing ends at t = 10 min. Sampling of tensile bars starts at t = 20 min.

Fig. 6. Density index as a function of time during degassing and isothermal holding for the different degassing methods. Degassing ends at t = 10 min. Sampling of tensile bars starts at t = 20 min.

Fig. 7. Correlation between density index (DI) and hydrogen (H) content in the melt for the three degassing methods used in this study.

Fig. 8. Porosity in the RPT samples solidified under partial vacuum. (a) before degassing; and during degassing: (b) rotary, 2 min; (c) rotary, 5 min; (d) rotary, 10 min; (e) HSMC, 2 min; (f) HSMC, 5 min.

Fig. 9. Pore size distribution of the RPT samples solidified under vacuum during degassing.

Fig. 10. Micrographs of the dross collected after melt treatment by (a) rotary and (b) HSMC degassing.

Fig. 11. Representative microstructure of the tensile bars before testing for each degassing method. Samples obtained at 10 min after degassing. (a) tablet; (b) rotary and (c) HSMC degassing.

Fig. 12. Tensile properties of the tensile specimens as a function of holding time after degassing. (a) yield strength (YS) and ultimate tensile strength (UTS) and (b) elongation at break.

Fig. 13. Fracture surfaces of the post-mortem tensile bars cast at 10min after degassing. (a) tablet degassing; (b) rotary degassing; (c) HSMC degassing. (d-f) Vertical sections of samples in (a-c).

Fig. 14. SEM micrographs showing the oxide films on the fracture surface of the tensile specimens. (a) tablet degassing; (b) rotary degassing; (c) HSMC degassing.

Fig. 15. Area fraction of defects at fracture surface (f) as a function of holding time after degassing.

Fig. 16. Tensile properties as a function of the fraction of defects at fracture surface for (a) UTS; (b) Elongation.